Nanoscale

PAPER

View Article Online
View Journal | View Issue

Cite this: *Nanoscale*, 2018, **10**, 13607

Understanding quantum emitters in plasmonic nanocavities with conformal transformation: Purcell enhancement and forces

V. Pacheco-Peña [a] and M. Navarro-Cía *[b]

Nanogaps supporting cavity plasmonic modes with unprecedented small mode volume are attractive platforms for tailoring the properties of light–matter interactions at the nanoscale and revealing new physics. Hitherto, there is a concerning lack of analytical solutions to divide the complex interactions into their different underlying mechanisms to gain a better understanding that can foster enhanced designs. Bowtie apertures are viewed as an effective and appealing nanocavity and are studied here within the analytical frame of conformal transformation. We show how the non-radiative Purcell enhancement of a quantum emitter within the bowtie nanocavity depends strongly not only on the geometry of the nanocavity, but also on the position and orientation of the emitter. For a 20 nm diameter (ø 20 nm) bowtie nanocavity, we report a change of up to two orders of magnitude in the maximum non-radiative Purcell enhancement and a shift in its peak wavelength from green to infra-red. The changes are tracked down to the overlap between the emitter field and the gap plasmon mode field distribution. This analysis also enables us to understand the self-induced trapping potential of a colloidal quantum dot inside the nanocavity. Since transformations can be cascaded, the technique introduced in this work can also be applied to a wide range of nanocavities found in the literature.

Received 22nd February 2018,
Accepted 19th June 2018

DOI: 10.1039/c8nr01527a

rsc.li/nanoscale

Introduction

Plasmonics is a thriving research field that has created transformative opportunities for a wide range of applications, spanning from spectroscopy to photothermal therapy.[1] The intrinsic nanoscopic volume and high sensitivity to the local environment of surface plasmon modes enable label-free molecular detection.[2–5] The large near-field intensity gradients in plasmonic structures yield amplified optical forces that can be used for nanoparticle manipulation (*i.e.*, nanotweezers).[6–10] These strong electromagnetic fields also allow weak nonlinear processes, which are governed by the local field, to be notably enhanced.[11–14] The ability of plasmons to surpass the diffraction limit is used to produce super-resolution images and to push the resolution of nanolithography.[15–19] By the proper engineering of plasmonic structures, light can be trapped and absorbed efficiently in thin-film solar cells.[20,21] Gold nanoparticles convert efficiently photon energy into local heat that is used for selective tumour apoptosis.[22]

Benefitting from the advancements in nanofabrication and the possibility of creating metal–insulator–metal configurations supporting gap plasmon modes, plasmonics is also becoming a fascinating platform to study the nanoscale world.[23–26] In this quest, the preferred cavity is the so-called particle(s)-on-a-mirror,[5,27–31] but apertures in metals have also their own merits. As far as spectroscopy and trapping are concerned, apertures can remove large background signals and are a natural trapping environment.[2,6,9,10,32–34]

Nowadays, to design plasmonic nanostructures for specific applications and to build knowledge from experimental observations, scientists rely strongly on a heavy computational burden[35] since analytical solutions are limited to simple geometries like spheres.[36] The challenge lies then in mapping the plasmon resonances and the corresponding field distributions analytically for the more complex nanostructures and assemblies whereby physical understanding can be gained and a blueprint for the design of new plasmonic nanostructures is provided. An analytical tool that holds promise in this regard is transformation optics.[37,38] It has been championed for open-crescent-shaped[39–41] and several dimer nanoantennas (*e.g.*, spheres,[42] cylinders,[43] cylindrical sectors,[44] bowties[45] and tripods[46]), but its application in nanocavities is limited to canonical ring-disk and crescent-shaped nanocavities.[37,47,48]

[a]*Emerging Technology and Materials group, School of Engineering, Newcastle University, Merz Court, Newcastle Upon Tyne NE1 7RU, UK*
[b]*School of Physics and Astronomy, University of Birmingham, Birmingham, Edgbaston, B15 2TT, UK. E-mail: m.navarro-cia@bham.ac.uk*

Motivated by the lack of analytical solutions in plasmonic nanocavities and the increasing use of bowtie nanocavities for trapping and molecular fluorescence,[2,9,10,33] we report here an analytical solution for the Purcell enhancement and forces experienced by an emitter (*e.g.*, colloidal quantum dot, QD) inside a two-dimensional (2D) bowtie nanocavity (*i.e.*, a 3D bowtie nanocavity with *z*-invariance). The study of bowtie nanocavities is timely given their popularity in the community arisen from their stronger field concentration and hence field enhancement at their centre as well as their strong coupling to light compared to other nanocavities.[2,9]

Analytical framework

A schematic of the bowtie nanocavity to be investigated in this manuscript can be found in Fig. 1a. Note that it can be understood as a ring-bowtie nanoantenna or as a mirror-image nanoepsilon.[49] Without loss of generality, gold is considered for the metal parts of the nanocavity. L'_1 and L'_2 correspond to the distances from the bowtie nanocavity inner arms (radius of 10 nm) and the 0.5 mm long connecting taper to a circumference of radius 1 nm, as shown in Fig. 1a. The ring width is chosen to be Δ'_t = 10 nm to avoid plasmon hybridization[50] in the ring, as is demonstrated in Fig. 1c and d. Effectively, this is equivalent to having a single nanocavity embedded in gold; hence, Δ'_t = 10 nm and Δ'_t = infinite match in Fig. 1c and d.

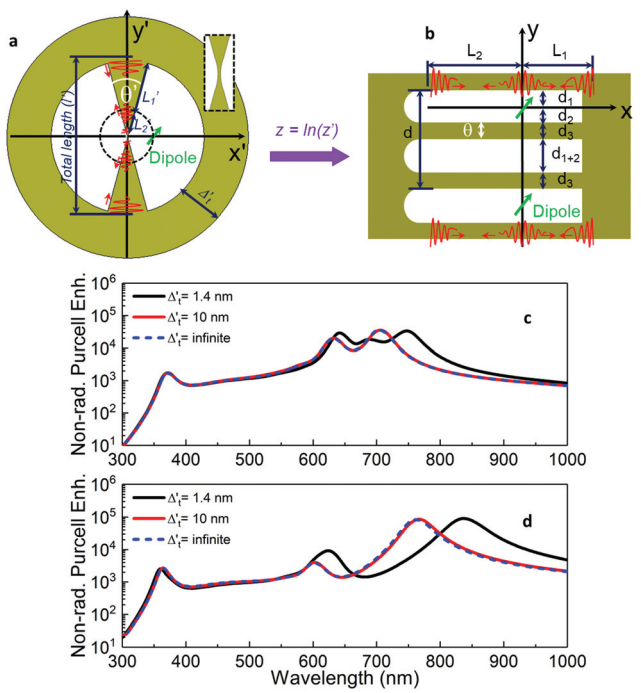

Fig. 1 (a) A nanoemitter inside a mirror-image gold nanoepsilon (*i.e.*, bowtie nanocavity). (b) The corresponding transformed space obtained after applying the conformal mapping indicated in the figure. (c, d) Numerical results of the non-radiative Purcell enhancement for different values of Δ'_t when the dipole is oriented horizontally (c) and vertically (d).

The flare angle θ' will be varied throughout the manuscript. The gradual connection between the metal inner parts (*i.e.*, the taper) follows a Bézier polygon starting at 0.5 nm from the centre of the nanocavity. The position and orientation of the point (*e.g.*, dimensionless) dipole source (translationally invariant along the out-of-plane direction) mimicking a nanoemitter inside the bowtie nanocavity will be also varied.

Since the diameter of the nanocavity is l' = 20 nm $\ll \lambda_0$, the problem can be treated quasi-statically. In this scenario, the electric and magnetic fields are decoupled and the former can be completely described by an electrostatic potential satisfying Laplace's equation $\nabla^2\varphi'(x', y') = 0$.

The bowtie nanocavity shown in Fig. 1a can be transformed into the geometry shown in Fig. 1b by applying the conformal transformation $z = \ln(z'/a)$.[11,45,46] Here $z = x + iy$ and $z' = x' + iy'$ correspond to the spatial coordinates in the transformed and original frames, respectively, and a is the distance between the emitter and the origin of the coordinates. With this conformal mapping, the arbitrary oriented line dipole source and the bowtie nanocavity are transformed into a periodic multislab structure with an array of line dipoles located every two slabs. Hence, the periodic unit cell (with a 2π periodicity along the y axis) consists of an array of line dipoles and two metallic slabs (connected at their ends). The dimensions of the metallic slabs are defined by $L_1 + L_2$ and θ (= d_3) along the x and y axes, respectively.

An important consequence of the quasi-static treatment of the nanocavity and the applied conformal mapping that preserves the local angles is that the material properties are identical in both transformed and original frames. Additionally, the potential is preserved $\phi(x,y) = \phi'(x',y')$ in both scenarios, respectively.[37] Hence, the underlying physics governing Fig. 1a is identical to that of Fig. 1b. Given its canonical form, the description of the latter is simpler and, thus, is given next. From Fig. 1b one can expect that the array of dipoles will excite surface plasmons (SPs) propagating along the x axis. Since the slabs have finite length (L_1 and L_2), the SPs will be reflected back and forth, producing standing-wave patterns that one can identify to localized surface plasmon (LSP) modes, *i.e.*, the eigen-modes of the system. Because of the small size of the nanocavity compared to the incident wavelength, radiation losses are negligible and the energy pumped into the system by the emitter is dissipated into the metal due to absorption. The quantitative results will be shown and discussed in the following sections and the complete analytical solution in the transformed space can be found in the Methods section.

Results and discussion

The number and spectral position of localized surface plasmon modes

The resonant performance of the bowtie nanocavity can be evaluated analytically by simply solving the problem in the periodic multislab frame.[44–46,51] Because of the finite physical size of the nanostructure under study, the LSP modes for the

bowtie nanocavity will be distributed in the spectrum at discrete wavelengths satisfying the following resonant condition (see the Methods section for more details):

$$\left\{[\varepsilon_{\mathrm{Au}}(\omega)-1]^2\left[e^{k(3d_1+3d_2+2d_3)}-e^{k(d_1+4d_2+4d_3)}\right]\right.$$
$$\left.-[\varepsilon_{Au}(\omega)+1]^2\left[e^{k(d_1+4d_2+2d_3)}-e^{k(3d_1+6d_2+4d_3)}\right]\right\}^2 \quad (1)$$
$$-\left\{2\left[\varepsilon_{Au}(\omega)^2-1\right]\left[e^{k(3d_1+6d_2+3d_3)}-e^{k(d_1+4d_2+3d_3)}\right]\right\}^2=0$$

where $\varepsilon_{\mathrm{Au}}(\omega)$ is the permittivity of gold, $\omega = 2\pi c/\lambda_0$ is the angular frequency, c is the velocity of light in vacuum, λ_0 is the operational wavelength and k is the angular momentum for each LSP mode defined as $k = (n\pi - \Delta\varphi)(L_1 + L_2)^{-1}$ (with n = 1, 2, 3...). $\Delta\varphi$ is the extra phase required to take into account non-perfect reflections of the SP modes at both ends of the metallic slabs along the x axis (see the Methods section).

By applying the above resonant condition, the number of LSP modes supported by the bowtie nanocavity as a function of the angular aperture of the arms ($\theta' = \theta = d_3$) are shown in Fig. 2a for vertical and horizontal emitter orientations. As observed, the number of modes increases for smaller θ'. This is an expected result since there is a clear dependence on the dimension θ' (= d_3) for fixed L_1 and L_2, in agreement with our recent findings for bowtie nanoantennas.[45,51] To further study the plasmonic resonances of the nanocavity, the spectral distributions of the first 10 LSP modes for nanocavities with θ' = 20°, 35° and 45° under vertical and horizontal emitter orientations are depicted in Fig. 2b and c, respectively. As is shown, the LSP modes are located within the entire visible spectrum and they are blue shifted when θ' is increased, similarly to canonical multilayer plasmonic systems. Also, it can be observed that higher-order LSP modes (n > 3) are agglomerated close to the SP wavelength λ_{sp}. It is worth underlining that the LSP modes are eigen-modes of the nanocavity and their emergence and strength will depend on their field overlap integral to the emitter. The role of the emitter position and orientation will be discussed in the following sections.

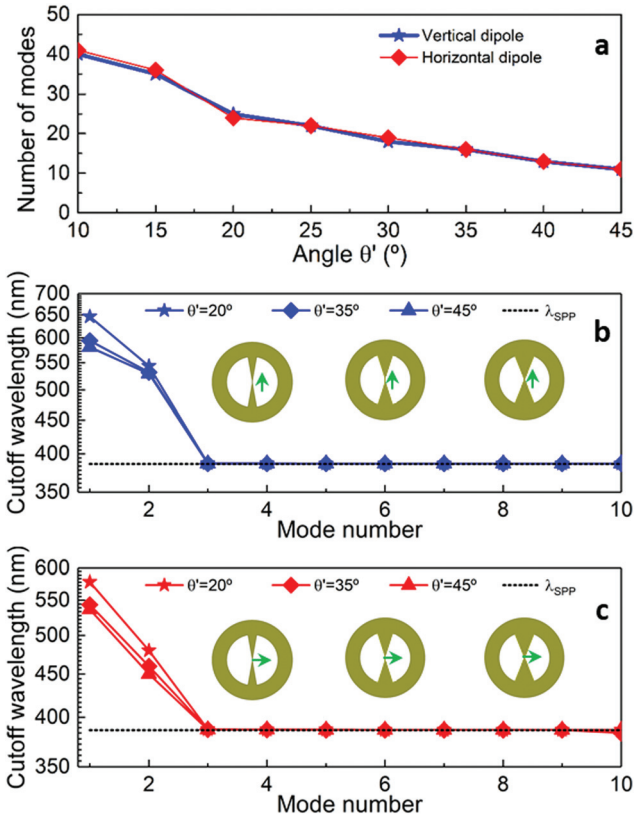

Fig. 2 (a) The number of LSP modes supported by the nanocavity as a function of θ' for both vertical and horizontal emitter orientations. (b) Analytical resonant wavelength for the LSP modes supported by bowtie nanocavities with angles θ' = 20° (stars), 35° (rhombus) and 45° (triangles), excited under vertical (b) and horizontal (c) emitter orientations, as shown in the insets. Note that the discrete points have been connected with solid lines to guide the eye. Horizontal dashed lines mark the λ_{sp}.

Non-radiative Purcell enhancement and field distribution

Within the conformal transformation and quasi-static formalisms, the power dissipated in the original scenario, $P_{\mathrm{abs}}^{(x',y')}$, is identical to that in the transformed space, $P_{\mathrm{abs}}^{(x,y)}$. The latter can be easily calculated by evaluating the electric field at the position of the dipole as $P_{\mathrm{nr}} = -(1/2)\omega\mathrm{Im}\left\{p_x^* E_{1x}^S(x,y) + p_y^* E_{1y}^S(x,y)\right\}$ where P_{nr} is the non-radiative power emission, p_x and p_y are x and y components of the dipole moment with magnitude $|p|$, respectively, and $E_{1x}^S(x,y)$ and $E_{1y}^S(x,y)$ are the x and y components of the electric field in the region where the dipole is located (see the Methods section for the full analytical expression). Based on this, the non-radiative Purcell enhancement can be calculated as $\overline{\Gamma_{\mathrm{nr}}} = P_{\mathrm{nr}}(\omega)/P_0(\omega)$ where $P_0(\omega) = (1/16)\omega^3\mu_0|p|^2$ is the power radiated by the emitter and μ_0 is the permeability of vacuum. It is important to note that, since the nanocavity is evaluated quasi-statically, the extinct power by a point dipole has been used to describe the non-radiative power of the emitter. Moreover, in all the calculations presented here, an intrinsic quantum yield equal to 1 has been used for the emitter in order to be able to relate the non-radiative decay of the emitter with the power absorbed by the nanocavity, $P_{\mathrm{nr}} = P_{\mathrm{abs}}^{(x,y)} = P_{\mathrm{abs}}^{(x',y')}$.[45,46]

With this formulation, the analytical results of the non-radiative Purcell enhancement spectra for a bowtie nanocavity with l' = 20 nm as a function of θ' (ranging from 10° to 45°) are shown in Fig. 3a and b considering vertical and horizontal emitter orientations, respectively. Here, the emitter is placed at (x' = 1 nm, y' = 0) in the original frame [*i.e.*, (x = y = 0) in the multislab geometry]. As observed, the LSP modes are blue shifted when θ' is increased, in agreement with the results shown in Fig. 2, covering the entire visible spectrum. For instance, the fundamental LSP mode (n = 1) is shifted from (infra-) red ~770 nm to yellow ~582 nm when θ' is modified from 10° to 45°, respectively, under a vertical emitter orientation. Similarly, it is displaced from red ~707 nm to green ~527 nm for the same range of θ' under the horizontal emitter orientation. To better observe this performance, the analytical

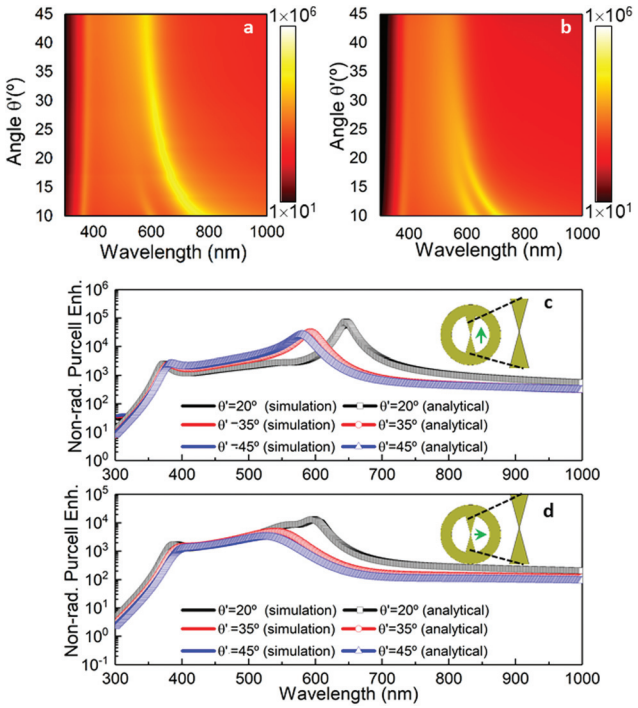

Fig. 3 Analytical $\overline{\Gamma_{nr}}$ for the bowtie nanocavity with varying θ' under vertical (a) and horizontal (b) emitter orientations. Numerical (solid lines) and analytical (symbols) results comparing the specific bowtie nanocavity with θ' = 20, 35, and 45° under vertical (c) and horizontal (d) emitter orientations.

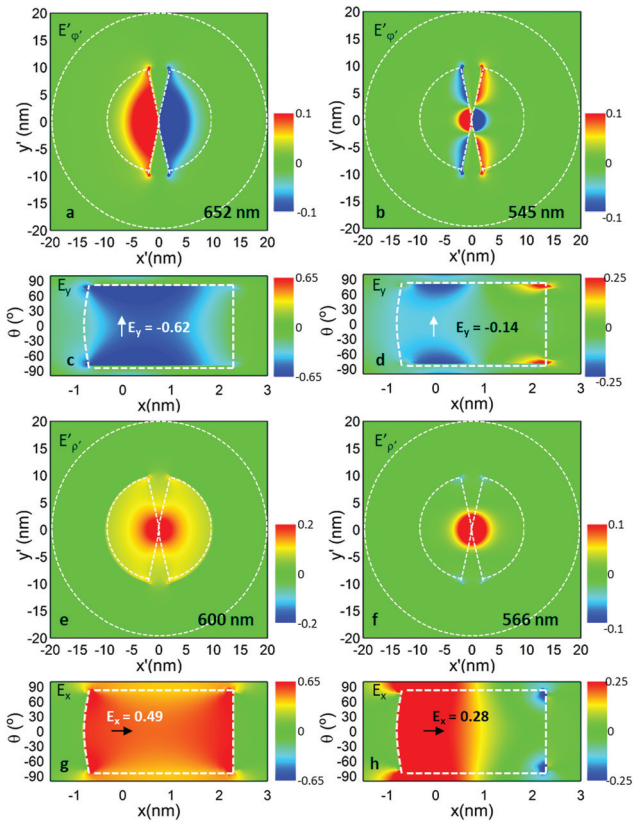

Fig. 4 Electric field distribution $E_{\varphi'}(x', y')$ and $E_{\rho'}(x', y')$ of the first two LSP modes for θ' = 20° under vertical (a, b) and horizontal (e, f) emitter orientations, respectively. Note that the colour scale has been saturated in order to better appreciate the field distribution. The corresponding electric field distributions $E_y(x, y)$ and $E_x(x, y)$ in the transformed space for vertical (c, d) and horizontal (g, h) emitter orientations.

results of the non-radiative Purcell enhancement spectra for values of θ' = 20°, 35° and 45° are shown in Fig. 3c and d considering vertical and horizontal emitter orientations, respectively. The analytical results are compared with numerical simulations carried out with the commercial software COMSOL Multiphysics® (see the Methods section) for the original bowtie nanocavity space. The good agreement achieved between analytical and numerical results validates the analytical formulation.

As observed in Fig. 3, the magnitude of the non-radiative Purcell enhancement is different for each emitter orientation and LSP mode. This stems from the different field integral overlap between the emitter and the LSP field mode distribution. The larger the field integral overlap is, the higher the non-radiative Purcell enhancement is. To investigate this in more detail, the results of the field distribution in the bowtie nanocavity for the fundamental (n = 1) and first higher-order (n = 2) LSP modes under vertical and horizontal emitter orientations are shown in Fig. 4 for θ' = 20°. Note that E_y in the multislab geometry corresponds to the azimuthal component of the electric field ($E'_{\varphi'}$) in the original frame, whereas E_x in the multislab geometry relates to the radial component of the electric field ($E'_{\rho'}$) in the original frame.[45,46] Hence, for vertical (Fig. 4a and b) and horizontal emitter orientations (Fig. 4e and f), $E'_{\varphi'}$ and $E'_{\rho'}$ are plotted accordingly. Here, $E'_{\varphi'}$ and $E'_{\rho'}$ are calculated as $E'_{\varphi'} = -E'_{x'}\sin(\varphi') + E'_{y'}\cos(\varphi')$ and $E'_{\rho'} = E'_{x'}\cos(\varphi') + E'_{y'}\sin(\varphi')$ with $\varphi' = \tan^{-1}(y'/x')$, respectively.

Fig. 4 manifests unquestionably the differences between each LSP mode. For either emitter orientation, the first higher-order LSP mode displays an additional antinode in the field distribution compared to the fundamental mode. This is even more evident in the transformed space. For instance, under vertical emitter orientation, E_y at the first peak of $\overline{\Gamma_{nr}}$ has one antinode in between two nodes at the ends of the nanocavity (Fig. 4c), which corresponds to the first harmonic of the standing-wave pattern, *i.e.*, the field distribution associated with the fundamental n = 1 LSP mode. For the second peak (Fig. 4d) E_y has two antinodes and three nodes, accounting for the second harmonic of the standing-wave pattern, *i.e.*, the n = 2 LSP mode. For the horizontal emitter orientation, two E_x maxima are obtained at both ends with a node in between them at the first peak of $\overline{\Gamma_{nr}}$ (Fig. 4g), while the field distribution for the second peak (Fig. 4h) has a node in between a maximum and a minimum at the ends of the nanocavity.

The field representation in the transformed space also assists in the discussion regarding the magnitude of $\overline{\Gamma_{nr}}$. For the vertical emitter orientation (Fig. 4a–d), the emitter [at (x', y') = (1, 0) in the real space, and (x, y) = (0, 0) in the transformed space] is located at a position where the field strength

of the $n = 1$ LSP mode is larger ($E_y = -0.62$) than that of the $n = 2$ LSP mode ($E_y = -0.14$). The field integral overlap is therefore larger for $n = 1$, resulting in a higher $\overline{\Gamma_{nr}}$ (as shown in Fig. 3c). The same argument applies to the horizontal emitter orientation case (Fig. 4e–h).

Changing the position of the emitter

To further study the influence of the emitter on $\overline{\Gamma_{nr}}$, $\overline{\Gamma_{nr}}$ is plotted against the emitter position along the x' axis in Fig. 5c and d under vertical and horizontal emitter orientations, respectively. These analytical results are in agreement with numerical simulations depicted in Fig. 5e and f. The peak of $\overline{\Gamma_{nr}}$ related to the fundamental LSP is visible regardless of the emitter orientation and position, but its magnitude is enhanced for positions closer to the centre for vertical emitter orientation, whereas it is more constant for horizontal emitter orientation. Namely, for $n = 1$ LSP mode, $\overline{\Gamma_{nr}}$ is equal to 1.11×10^6, 0.72×10^3 and 9.5×10^3 for vertical emitter orientation and 6.45×10^4, 1.3×10^3 and 1.6×10^3 for horizontal emitter orientation at $x' = 0.3$ nm, $x' = 6.6$ nm and $x' = 9.6$ nm, respectively. These gradient responses in $\overline{\Gamma_{nr}}$ for vertical and horizontal emitter orientations account for the strong and weak asymmetric field distributions of the $n = 1$ LSP mode in Fig. 4c and g, respectively, and also reflect the significant contribution of higher-order LSP modes for $x' \to 0$ and 10 nm; emitters placed close to metal boundaries (either by the nanocavity centre or by its outer periphery) couple more efficiently to the higher-order LSP modes that are accumulated at such boundaries (see the wavelength range below 600 nm in Fig. 4c–f).[29,42] These additional non-radiative channels contribute to the total $\overline{\Gamma_{nr}}$, yielding an overall increase of the $\overline{\Gamma_{nr}}$ baseline.

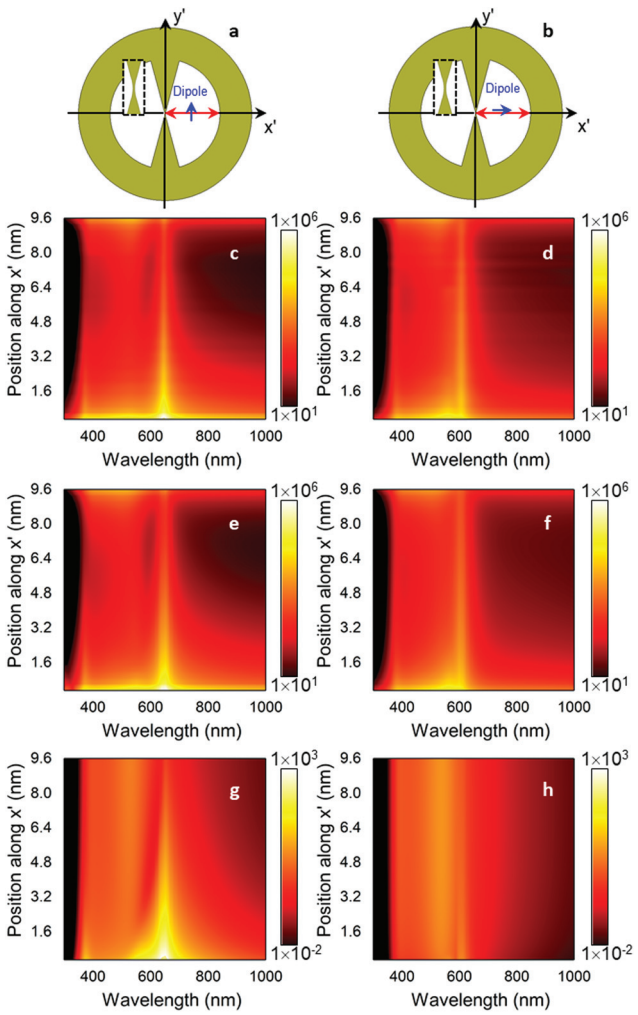

Fig. 5 Schematic representation of the bowtie nanocavity with a vertical (a) and a horizontal emitter (b). Analytical (c, d) and numerical (e, f) $\overline{\Gamma_{nr}}$ for the bowtie nanocavity with $\theta' = 20°$ and a vertical (c, e) and a horizontal emitter (d, f) at $y' = 0$ and moving along the x' axis. Numerical $\overline{\Gamma_r}$ for vertical (g) and horizontal emitter orientations (h).

The impact of the emitter position is more significant for higher-order LSP modes, whose field distributions display nodes across the nanocavity and is enhanced at metal/dielectric interfaces (Fig. 4d and h). These higher-order LSP modes emerge in the spectral range ~370–570 nm (Fig. 2b and c) and are responsible for the increase in $\overline{\Gamma_{nr}}$ within such an approximate wavelength range at both ends of the spatial window displayed (Fig. 5c–f).

Additionally, the numerical results of the radiative Purcell spectra $\overline{\Gamma_r}$ (calculated as the power radiated by the bowtie nanocavity, P_r, normalized to the power radiated by the emitter P_0) as a function of the position of the emitter are shown in Fig. 5g and h for vertical and horizontal emitter orientations, respectively. These results show that $\overline{\Gamma_r}$ is three orders of magnitude lower than $\overline{\Gamma_{nr}}$, and thus, sustains the initial assumption of the theoretical frame that radiation losses are negligible in the system. From these results, one can also note that higher-order LSP modes have negligible radiative character compared to $n = 1$ LSP mode, since they are not dipolar in nature unlike the fundamental LSP mode.

For the sake of completeness, the analytical results of the $\overline{\Gamma_{nr}}$ when the emitter moves along the y' axis at $x' = 2.6$ nm are shown in Fig. 6c and d along with the numerical results (Fig. 6e and f). As observed, the magnitude of the $\overline{\Gamma_{nr}}$ for the different LSP modes is enhanced when the emitter is close to the metal (as was shown when the emitter was moved along the x' axis in Fig. 6c–f). For instance, for the LSP with $n = 1$, the $\overline{\Gamma_{nr}}$ is 8.95×10^3 and 6.54×10^4 for vertical emitter orientation and 4.22×10^3 and 2.29×10^4 for horizontal emitter orientation at $y' = 0$ nm and $y' = 9.6$ nm, respectively. Finally, the results of $\overline{\Gamma_r}$ are shown in Fig. 6g and h with, again, values three orders of magnitude lower than $\overline{\Gamma_{nr}}$, as in Fig. 5g and h.

Optical forces

As discussed above, the emitter excites bowtie nanocavity LSP modes. The field distributions induced by such LSP modes inside the nanocavity exert back then an optical force on the emitter. To consider this picture realistically, the emitter is assumed in this section to be a 2 nm diameter (∅ 2 nm) colloidal ZnO QD[52,53] and the nanocavity is filled with water ($\varepsilon_r = 1.77$). Note that the emitter model also takes into account the influence of the emitter on the nanocavity electric field that

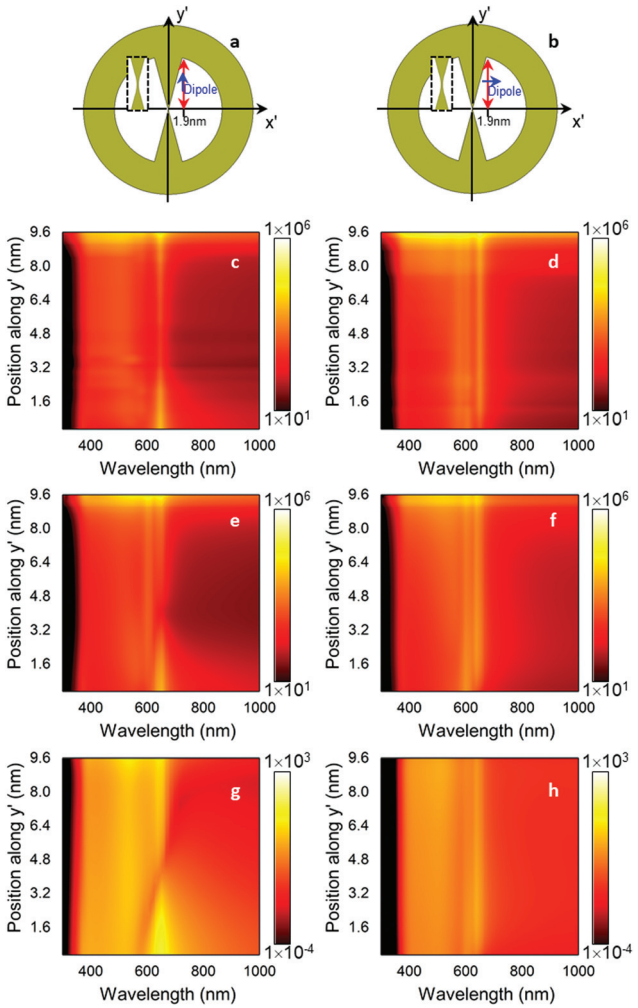

Fig. 6 Schematic representation of the bowtie nanocavity with a vertical (a) and a horizontal emitter (b). Analytical (c, d) and numerical (e, f) $\overline{\Gamma_{nr}}$ for the bowtie nanocavity with $\theta' = 20°$ and a vertical (c, e) and a horizontal emitter (d, f) at $x' = 2.6$ nm and moving along the y' axis. Numerical $\overline{\Gamma_r}$ for vertical (g) and horizontal emitter orientations (h).

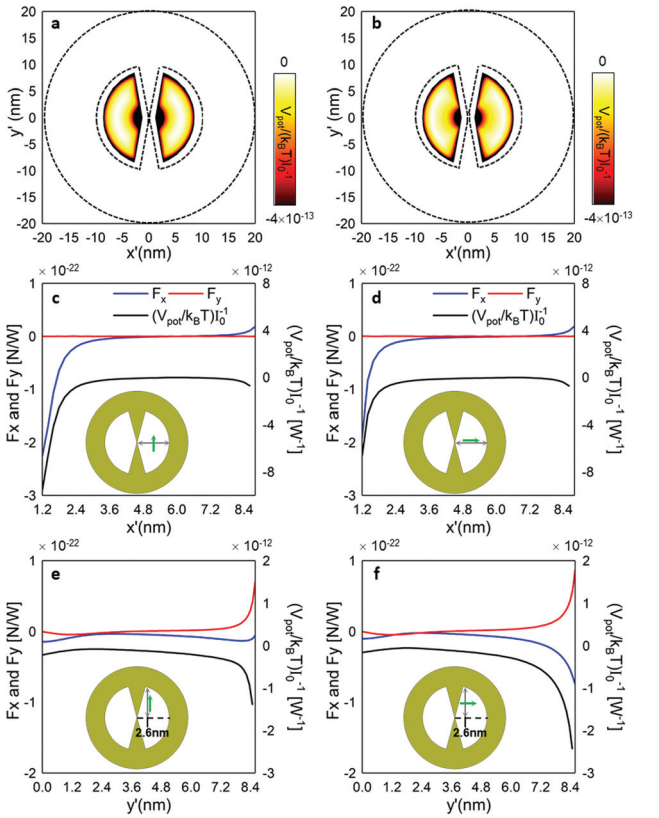

Fig. 7 (a, b) The normalized self-induced trapping potential distribution of a ∅ 2 nm colloidal ZnO QD inside a $\theta' = 20°$ nanocavity at the LSP resonant wavelength of 779.2 nm – photoluminescence polarized vertically – (a) and 697.7 nm – photoluminescence polarized horizontally – (b). (c, d) Normalized forces along the x (F_x) and y (F_y) axes (blue and red lines, respectively) together with the normalized self-induced trapping potential (black line) calculated at the $y' = 0$ horizontal line as shown in the insets for the photoluminescence polarized vertically (c) and photoluminescence polarized horizontally (d). (e, f) Normalized forces along the x (F_x) and y (F_y) axes (blue and red lines, respectively) together with the normalized self-induced trapping potential (black line) calculated at $x' = 2.6$ nm vertical line as shown in the insets for the photoluminescence polarized vertically (e) and photoluminescence polarized horizontally (f).

was neglected previously with the point dipole definition. We calculate the optical force $\langle F \rangle$ at the fundamental LSP mode wavelength using the Maxwell stress tensor through the electric field distribution.[6] In order to evaluate the stability of the trapping, we compute the potential energy of the colloidal ZnO QD in the field of the nanocavity as $V_{pot}(z') = -\int \langle F(z_1) \rangle dz_1$. Given the aqueous environment, Brownian motion should be taken into account. Hence, the potential is normalized to k_BT, where k_B is the Boltzmann constant and T the temperature, which is taken to be 300 K.

The spatial potential depth for the QD with vertical and horizontally polarized photoluminescence is shown in Fig. 7a and b, respectively. The x'-axis ($y' = 0$) and y'-axis ($x' = 2.6$ nm) cut is provided in Fig. 7c, d and e, f respectively, along with the optical forces to facilitate the discussion. Stable trapping is expected to occur along the perimeter of the nanocavity, especially close to the centre of the nanocavity where the field gradient is larger. Indeed, since stable trapping often requires a trap depth of $\sim 10 k_BT$,[54] only the centre of the nanocavity and the top and bottom vertexes provide a suitable spot, given the dimensions of the QD. From this, it also follows that an unpolarized QD placed along the $x' = 2.6$ nm vertical line will experience a force strong enough to be trapped at $y' = 0$ nm (towards the nanoantenna centre). When the QD approaches the nanoantenna vertices, it will also be trapped, but it will lean against the right or left metallic wall depending on the photoluminescence polarization (Fig. 7e and f).

Methods

Transformed space

Since the diameter of the Au bowtie nanocavity is significantly smaller than the operational wavelength ($l' \ll \lambda_0$), the quasi-

static approximation is applicable. In this scenario, the electric field can be fully described by an electrostatic potential satisfying Laplace's equation. In the geometry shown in Fig. 1b, the emitters are able to excite SP modes in both longitudinal and transversal directions, propagating along the y- and x-axes, respectively. However, since we are interested in calculating the surface plasmon modes for the multislab geometry when $L_1 + L_2 \ll \theta'$, the contribution of the longitudinal LSP modes can be neglected and it can be assumed that the excited LSP modes are mainly due to the transversal modes (with a phase variation along the x axis).

With these considerations taken into account, the electrostatic potentials outside and inside the metallic slabs in Fig. 1b can be calculated as the sum of all discrete transverse modes, as follows:

$$\sum_k \left[\frac{1}{1-e^{2ik(L_1+L_2)+i\Delta\varphi_1+i\Delta\varphi_2}}\left(e^{ikx}-e^{-ikx+2ikL_1+i\Delta\varphi_1}\right)\times\left(A_+e^{-ky}+B_+e^{-ky}+B_-e^{ky}\right)\right], 0<y<d_1 \quad (2)$$

$$\sum_k \left[\frac{1}{1-e^{2ik(L_1+L_2)+i\Delta\varphi_1+i\Delta\varphi_2}}\left(e^{ikx}-e^{-ikx+2ikL_1+i\Delta\varphi_1}\right)\times\left(A_-e^{ky}+B_+e^{-ky}+B_-e^{ky}\right)\right], -d_2<y<0 \quad (3)$$

$$\sum_k \left[\frac{1}{1-e^{2ik(L_1+L_2)+i\Delta\varphi_1+i\Delta\varphi_2}}\left(e^{ikx}-e^{-ikx+2ikL_1+i\Delta\varphi_1}\right)\times\left(E_+e^{-ky}+E_-e^{ky}\right)\right], -(d_1+2d_2+d_3)<y<-(d_2+d_3) \quad (4)$$

$$\sum_k \left[\frac{1}{1-e^{2ik(L_1+L_2)+i\Delta\varphi_1+i\Delta\varphi_2}}\left(e^{ikx}-e^{-ikx+2ikL_1+i\Delta\varphi_1}\right)\times\left(C_+e^{-ky}+C_-e^{ky}\right)\right], -(d_1+2d_2+2d_3)<y<-(d_1+2d_2+d_3) \quad (5)$$

$$\sum_k \left[\frac{1}{1-e^{2ik(L_1+L_2)+i\Delta\varphi_1+i\Delta\varphi_2}}\left(e^{ikx}-e^{-ikx+2ikL_1+i\Delta\varphi_1}\right)\times\left(D_+e^{-ky}+D_-e^{ky}\right)\right], -(d_2+d_3)<y<-d_2 \quad (6)$$

where A_+ and A_- are the expansion coefficients of the incident potential, B_+ and B_- are the coefficients due to the scattering potential in the region where the dipole is present ($d_2 < y < d_1$), E_+ and E_- are the coefficients associated with the scattering potential in the region where the dipole is absent ($d_2 + d_1$) and C_+, C_-, D_+ and D_- are those corresponding to the potential inside the metallic slabs (d_3); $\Delta\varphi_1$ and $\Delta\varphi_2$ are the phase corrections accounting for the complex reflection of the SP at the right and left gold walls of the transformed space, respectively; k is the wave number of the transverse LSP modes calculated as:

$$k = \frac{(n\pi - \Delta\varphi)}{L_1 + L_2} \quad (7)$$

with n = 1, 2, 3... representing each discrete LSP mode and $\Delta\varphi$ as the total phase correction applied to the bowtie nanocavity accounting for the complex reflection of the SP at both ends

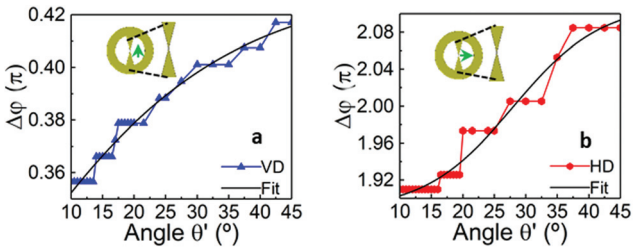

Fig. 8 Phase correction as a function of θ' considering a bowtie nanocavity with l' = 20 nm under vertical (a) and horizontal (b) polarization of the emitter.

of the nanostructure as described in the main text. For completeness, the calculated values of $\Delta\varphi$ for the nanocavities described in Fig. 3a and b with θ' ranging from 10° to 45° under vertical and horizontal emitter orientations are shown in Fig. 8a and b, respectively. As observed, the higher θ' is, the larger the value of $\Delta\varphi$ is. For each emitter orientation (vertical and horizontal), $\Delta\varphi(\theta')_{v,h}$ can be mathematically described with a sigmoidal function, as follows:

$$\Delta\varphi(\theta')_v = 0.43 - \frac{0.27}{\{1+e^{[18.54(\theta'+5.83)]}\}} \quad (8)$$

$$\Delta\varphi(\theta')_h = 2.11 - \frac{0.23}{\{1+e^{[7(\theta'-27.95)]}\}}. \quad (9)$$

Finally, the coefficients (A_+ and A_-) related to the incident potential can be calculated by expanding the potential of the dipole emitter along the x direction *via* a Fourier transform, as follows:

$$A_\pm = \frac{\pm p_y - ip_x \mathrm{sgn}(k)}{2\varepsilon_0} \quad (10)$$

where p_x and p_y are the two components of the dipole moment along the x- and y-axes, respectively, and ε_0 is the permittivity in vacuum.

In order to calculate the coefficients $B_\pm$, $C_\pm$, $D_\pm$ and $E_\pm$ in eqn (2)–(6) it is necessary to apply boundary conditions at the metal/dielectric interfaces.

The continuity of the tangential component of the electric field $E_\parallel = E_x$ at the boundaries d_1, d_2, $d_2 + d_3$ and $d_1 + 2d_2 + 2d_3$ leads to

$$A_+e^{-kd_1} + B_+e^{-kd_1} + B_-e^{kd_1} - C_+e^{k(d_1+2d_2+2d_3)} - C_-e^{-k(d_1+2d_2+2d_3)} = 0 \quad (11)$$

$$A_-e^{-kd_2} + B_+e^{kd_2} + B_-e^{-kd_2} - D_+e^{kd_2} - D_-e^{-kd_2} = 0 \quad (12)$$

$$E_+e^{k(d_2+d_3)} + E_-e^{-k(d_2+d_3)} - D_+e^{k(d_2+d_3)} - D_-e^{-k(d_2+d_3)} = 0 \quad (13)$$

$$E_+e^{k(d_1+2d_2+d_3)} + E_-e^{-k(d_1+2d_2+d_3)} - C_+e^{k(d_1+2d_2+d_3)} - C_-e^{-k(d_1+2d_2+d_3)} = 0 \quad (14)$$

The continuity of the normal component of the displacement current $D_\perp = D_y = \varepsilon_{Au}E_y$ across the same boundaries as the expressions above leads to

$$A_+e^{-kd_1} + B_+e^{-kd_1} - B_-e^{kd_1} - \varepsilon_{Au}C_+e^{k(d_1+2d_2+2d_3)} + \varepsilon_{Au}C_-e^{-k(d_1+2d_2+2d_3)} = 0 \quad (15)$$

$$A_-e^{-kd_2} - B_+e^{kd_2} + B_-e^{-kd_2} + \varepsilon_{Au}D_+e^{kd_2} - D\varepsilon_{Au-}e^{-kd_2} = 0 \quad (16)$$

$$E_+e^{k(d_2+d_3)} - E_-e^{-k(d_2+d_3)} - \varepsilon_{Au}D_+e^{k(d_2+d_3)} + \varepsilon_{Au}D_-e^{-k(d_2+d_3)} = 0 \quad (17)$$

$$-E_+e^{k(d_1+2d_2+d_3)} + E_-e^{-k(d_1+2d_2+d_3)} + \varepsilon_{Au}C_+e^{k(d_1+2d_2+d_3)} - \varepsilon_{Au}C_-e^{-k(d_1+2d_2+d_3)} = 0 \quad (18)$$

with ε_{Au} being the permittivity of the metal (gold) used in the bowtie nanocavity. For the sake of brevity and due to the complexity of each constant, their solutions are not shown here. However, they can be easily obtained either manually or with the assistance of mathematical software.

The solutions of the potentials in real space for the region where the dipole is present (ϕ_1^S for $d_2 < y < d_1$) and absent (ϕ_2^S for $d_2 + d_1$) can be calculated by applying an inverse Fourier transform to the induced potentials, as follows:

$$\phi_1^S = \frac{1}{2\varepsilon_0(L_1+L_2)}\sum_n\{p_x[\sin(kx)+\sin(kx-2kL_1-\Delta\varphi_1)] + p_y[\cos(kx)-\cos(kx-2kL_1-\Delta\varphi_1)]\} \times (B_+e^{-ky}+B_-e^{ky}) \quad (19)$$

$$\phi_2^S = \frac{1}{2\varepsilon_0(L_1+L_2)}\sum_n\{p_x[\sin(kx)+\sin(kx-2kL_1-\Delta\varphi_1)] + p_y[\cos(kx)-\cos(kx-2kL_1-\Delta\varphi_1)]\} \times (E_+e^{-ky}+E_-e^{ky}) \quad (20)$$

Following the same steps for both metallic slabs, the expressions defining the potentials (ϕ_1^m and ϕ_2^m, which correspond to the top and bottom arms in the scenario of the bowtie nanocavity) are as follows:

$$\phi_1^m = \frac{1}{2\varepsilon_0(L_1+L_2)}\sum_n\{p_x[\sin(kx)+\sin(kx-2kL_1-\Delta\varphi_1)] + p_y[\cos(kx)-\cos(kx-2kL_1-\Delta\varphi_1)]\} \times \left(C_+e^{-ky}+C_-e^{ky}\right) \quad (21)$$

$$\phi_2^m = \frac{1}{2\varepsilon_0(L_1+L_2)}\sum_n\{p_x[\sin(kx)+\sin(kx-2kL_1-\Delta\varphi_1)] + p_y[\cos(kx)-\cos(kx-2kL_1-\Delta\varphi_1)]\} \times \left(D_+e^{-ky}+D_-e^{ky}\right) \quad (22)$$

From these results, the x and y components of the electric field outside and inside the metallic slabs can be calculated by simply differentiating the potentials defined in eqn (19)–(22):

$$E_{1x}^S = -\Lambda\sum_n\{p_x[\cos(kx)+\cos(kx-2kL_1-\Delta\varphi_1)] - p_y[\sin(kx)-\sin(kx-2kL_1-\Delta\varphi_1)]\} \times \left(B_+e^{-ky}+B_-e^{ky}\right) \quad (23)$$

$$E_{2x}^S = -\sum_n\{p_x[\cos(kx)+\cos(kx-2kL_1-\Delta\varphi_1)] - p_y[\sin(kx)-\sin(kx-2kL_1-\Delta\varphi_1)]\} \times \left(E_+e^{-ky}+E_-e^{ky}\right) \quad (24)$$

$$E_{1x}^m = -\Lambda\sum_n\{p_x[\cos(kx)+\cos(kx-2kL_1-\Delta\varphi_1)] - p_y[\sin(kx)-\sin(kx-2kL_1-\Delta\varphi_1)]\} \times \left(C_+e^{-ky}+C_-e^{ky}\right) \quad (25)$$

$$E_{2x}^m = -\sum_n\{p_x[\cos(kx)+\cos(kx-2kL_1-\Delta\varphi_1)] - p_y[\sin(kx)-\sin(kx-2kL_1-\Delta\varphi_1)]\} \times \left(D_+e^{-ky}+D_-e^{ky}\right) \quad (26)$$

$$E_{1y}^S = -\Lambda\sum_n\{p_x[\sin(kx)+\sin(kx-2kL_1-\Delta\varphi_1)] + p_y[\cos(kx)-\cos(kx-2kL_1-\Delta\varphi_1)]\} \times \left(-B_+e^{-ky}+B_-e^{ky}\right) \quad (27)$$

$$E_{2y}^S = -\Lambda\sum_n\{p_x[\sin(kx)+\sin(kx-2kL_1-\Delta\varphi_1)] + p_y[\cos(kx)-\cos(kx-2kL_1-\Delta\varphi_1)]\} \times \left(-E_+e^{-ky}+E_-e^{ky}\right) \quad (28)$$

$$E_{1y}^m = -\Lambda\sum_n\{p_x[\sin(kx)+\sin(kx-2kL_1-\Delta\varphi_1)] + p_y[\cos(kx)-\cos(kx-2kL_1-\Delta\varphi_1)]\} \times \left(-C_+e^{-ky}+C_-e^{ky}\right) \quad (29)$$

$$E_{2y}^m = -\Lambda\sum_n\{p_x[\sin(kx)+\sin(kx-2kL_1-\Delta\varphi_1)] + p_y[\cos(kx)-\cos(kx-2kL_1-\Delta\varphi_1)]\} \times \left(-D_+e^{-ky}+D_-e^{ky}\right) \quad (30)$$

where $\Lambda = k/[2\varepsilon_0(L_1+L_2)]$.

The resonant condition described in eqn (1) is derived taking into account the condition of divergence of the coefficients of the scattered potential ($B_\pm$) calculated from eqn (11)–(18).

Numerical simulations

The commercial finite element analysis software COMSOL Multiphysics® is used to validate the analytical results. Gold permittivity is modelled using an analytical polynomial equation. This function fits Palik's experimental data.[55] The bowtie nanocavities are embedded in vacuum (and gold in one specific case in Fig. 1c and d), modelled as a two-dimensional square 700 nm × 700 nm box enclosed by scattering boundary conditions (*i.e.*, perfectly matched layers). The emitter is mod-

elled using two anti-parallel in-plane magnetic currents with a separation of 5 pm. For the optical forces, the nanocavity is filled with water [ε_r(600 nm) = 1.77] and the colloidal ZnO QD is modelled as a circle of diameter 2 nm and dielectric function fitting Bodurov's experimental data.[56] A fine mesh is used with a maximum and a minimum element size of 2 nm and 3 pm, respectively, within the vacuum region. A refined mesh, twice smaller than in vacuum, is used for gold parts to ensure accurate results.

Conclusions

The conformal transformation technique has been applied to a bowtie nanocavity hosting a nanoemitter in order to describe analytically the non-radiative Purcell enhancement experienced by such local nanoemitters. The non-radiative decay channels in the system are the different LSP modes excited by the emitter. For a ∅ 20 nm gold bowtie nanocavity, multiple LSP modes emerge within the entire visible spectrum whose strength and spectral position depend strongly on the position and orientation of the emitter. The analysis presented here has also enabled us to investigate the self-induced trapping potential of a realistic ∅ 2 nm colloidal ZnO QD inside the ∅ 20 nm gold bowtie nanocavity. The trapping force exceeds the Brownian motion along the perimeter of the bowtie nanocavity regardless of the photoluminescence polarization. The results presented here underline the potential of conformal transformation to unveil the different underlying mechanisms in plasmonic systems and hold promise for outlining design guidelines for plasmonic-based trapping systems. In addition, the methodology can be applied in a straightforward manner to understand the quantum effects in bowtie nanocavities.[37] It should be noted that larger bowtie nanocavities have a significant radiative channel and the quasi-static approximation fails. Nevertheless, this study still provides general guidelines to predict qualitatively the forces experienced by a QD inside the nanocavity.

Conflicts of interest

There are no conflicts to declare.

Acknowledgements

V. P.-P. is supported by the Newcastle University [Newcastle University Research Fellow]. M. N.-C. is supported by the University of Birmingham [Birmingham Fellowship].

References

1 J. A. Schuller, E. S. Barnard, W. Cai, Y. Chul Jun, J. S. White and M. L. Brongersma, *Nat. Mater.*, 2010, **9**, 193.
2 G. Lu, W. Li, T. Zhang, S. Yue, J. Liu, L. Hou, Z. Li and Q. Gong, *ACS Nano*, 2012, **6**, 1438.
3 H. Aouani, H. Šipová, M. Rahmani, M. Navarro-Cía, K. Hegnerová, J. Homola, M. Hong and S. A. Maier, *ACS Nano*, 2013, **7**, 669.
4 H. Aouani, M. Rahmani, H. Šípová, V. Torres, K. Hegnerová, M. Beruete, J. Homola, M. Hong, M. Navarro-Cía and S. A. Maier, *J. Phys. Chem. C*, 2013, **117**, 18620.
5 A. R. L. Marshall, J. Stokes, F. N. Viscomi, J. E. Proctor, J. Gierschner, J.-S. G. Bouillard and A. M. Adawi, *Nanoscale*, 2017, **9**, 17415.
6 K. Okamoto and S. Kawata, *Phys. Rev. Lett.*, 1999, **83**, 4534.
7 M. Righini, P. Ghenuche, S. Cherukulappurath, V. Myroshnychenko, F. J. García de Abajo and R. Quidant, *Nano Lett.*, 2009, **9**, 3387.
8 W. Zhang, L. Huang, C. Santschi and O. J. F. Martin, *Nano Lett.*, 2010, **10**, 1006.
9 P. Mestres, J. Berthelot, S. S. Aćimović and R. Quidant, *Light: Sci. Appl.*, 2016, **5**, e16092.
10 M. Shah Alam, F. Karima and C. Zhao, *Nanoscale*, 2016, **8**, 9480.
11 M. Navarro-Cía and S. A. Maier, *ACS Nano*, 2012, **6**, 3537.
12 H. Aouani, M. Navarro-Cía, M. Rahmani, T. P. H. Sidiropoulos, M. Hong, R. F. Oulton and S. A. Maier, *Nano Lett.*, 2012, **12**, 4997.
13 M. Kauranen and A. V. Zayats, *Nat. Photonics*, 2012, **6**, 737.
14 H. Aouani, M. Rahmani, M. Navarro-Cía and S. A. Maier, *Nat. Nanotechnol.*, 2014, **9**, 290.
15 S. Kawata, Y. Inouye and P. Verma, *Nat. Photonics*, 2009, **3**, 388.
16 F. Balzarotti and F. D. Stefani, *ACS Nano*, 2012, **6**, 4580.
17 J. L. Ponsetto, F. Wei and Z. Liu, *Nanoscale*, 2014, **6**, 5807.
18 N. Fang, H. Lee, C. Sun and X. Zhang, *Science*, 2005, **308**, 534.
19 W. Srituravanich, L. Pan, Y. Wang, C. Sun, D. B. Bogy and X. Zhang, *Nat. Nanotechnol.*, 2008, **3**, 733.
20 H. A. Atwater and A. Polman, *Nat. Mater.*, 2010, **9**, 205.
21 S. Mubeen, J. Lee, W.-R. Lee, N. Singh, G. D. Stucky and M. Moskovits, *ACS Nano*, 2014, **8**, 6066.
22 G. Baffou and R. Quidant, *Laser Photonics Rev.*, 2013, **7**, 171.
23 Z. C. Dong, X. L. Zhang, H. Y. Gao, Y. Luo, C. Zhang, L. G. Chen, R. Zhang, X. Tao, Y. Zhang, J. L. Yang and J. G. Hou, *Nat. Photonics*, 2010, **4**, 50.
24 K. J. Savage, M. M. Hawkeye, R. Esteban, A. G. Borisov, J. Aizpurua and J. J. Baumberg, *Nature*, 2012, **491**, 574.
25 K. Santhosh, O. Bitton, L. Chuntonov and G. Haran, *Nat. Commun.*, 2016, **7**, 11823.
26 S. Trautmann, J. Aizpurua, I. Götz, A. Undisz, J. Dellith, H. Schneidewind, M. Rettenmayr and V. Deckert, *Nanoscale*, 2017, **9**, 391.
27 G. M. Akselrod, T. Ming, C. Argyropoulos, T. B. Hoang, Y. Lin, X. Ling, D. R. Smith, J. Kong and M. H. Mikkelsen, *Nano Lett.*, 2015, **15**, 3578.

28 T. B. Hoang, G. M. Akselrod and M. H. Mikkelsen, *Nano Lett.*, 2016, **16**, 270.
29 R. Chikkaraddy, B. de Nijs, F. Benz, S. J. Barrow, O. A. Scherman, E. Rosta, A. Demetriadou, P. Fox, O. Hess and J. J. Baumberg, *Nature*, 2016, **535**, 127.
30 F. Benz, M. K. Schmidt, A. Dreismann, R. Chikkaraddy, Y. Zhang, A. Demetriadou, C. Carnegie, H. Ohadi, B. de Nijs, R. Esteban, J. Aizpurua and J. J. Baumberg, *Science*, 2016, **354**, 726.
31 G.-C. Li, Y.-L. Zhang, J. Jiang, Y. Luo and D. Y. Lei, *ACS Nano*, 2017, **11**, 3067.
32 D. Punj, M. Mivelle, S. B. Moparthi, T. S. van Zanten, H. Rigneault, N. F. van Hulst, M. F. García-Parajo and J. Wenger, *Nat. Nanotechnol.*, 2013, **8**, 512.
33 A. A. Al Balushi, A. Zehtabi-Oskuie and R. Gordon, *Biomed. Opt. Express*, 2013, **4**, 1504.
34 Y. Zhao, D. Chen, H. Yue, M. M. Spiering, C. Zhao, S. J. Benkovic and T. J. Huang, *Nano Lett.*, 2014, **14**, 1952.
35 B. Gallinet, J. Butet and O. J. F. Martin, *Laser Photonics Rev.*, 2015, **9**, 577.
36 C. F. Bohren and D. R. Huffman, *Absorption and Scattering of Light by Small Particles*, Wiley-VCH Verlag GmbH, Weinheim, Germany, 1998.
37 A. Aubry and J. B. Pendry, *Active Plasmonics and Tunable Plasmonic Metamaterials*, John Wiley & Sons, Hoboken, NJ, US, 2013, ch. 4, pp. 105–152.
38 L. Xu and H. Chen, *Nat. Photonics*, 2015, **9**, 15.
39 Y. Luo, J. B. Pendry and A. Aubry, *Nano Lett.*, 2010, **10**, 4186.
40 A. I. Fernández-Domínguez, Y. Luo, A. Wiener, J. B. Pendry and S. A. Maier, *Nano Lett.*, 2012, **12**, 5946.
41 A. Aubry, D. Y. Lei, A. I. Fernández-Domínguez, Y. Sonnefraud, S. A. Maier and J. B. Pendry, *Nano Lett.*, 2010, **10**, 2574.
42 R.-Q. Li, D. Hernangómez-Pérez, F. J. García-Vidal and A. I. Fernández-Domínguez, *Phys. Rev. Lett.*, 2016, **117**, 107401.
43 A. Aubry, D. Y. Lei, S. A. Maier and J. B. Pendry, *Phys. Rev. Lett.*, 2010, **105**, 233901.
44 Y. Luo, D. Y. Lei, S. A. Maier and J. B. Pendry, *Phys. Rev. Lett.*, 2012, **108**, 023901.
45 V. Pacheco-Peña, M. Beruete, A. I. Fernández-Domínguez, Y. Luo and M. Navarro-Cía, *ACS Photonics*, 2016, **3**, 1223.
46 V. Pacheco-Peña, A. I. Fernández-Domínguez, Y. Luo, M. Beruete and M. Navarro-Cía, *Laser Photonics Rev.*, 2017, **11**, 170051.
47 J. B. Pendry, A. I. Fernández-Domínguez, Y. Luo and R. Zhao, *Nat. Phys.*, 2013, **9**, 518.
48 M. Kraft, Y. Luo and J. B. Pendry, *Nano Lett.*, 2016, **16**, 5156.
49 J.-Y. Lin, C.-Y. Tsai, P.-T. Lin, T.-E. Hsu, C.-F. Hsiao and P.-T. Lee, *Nanoscale Res. Lett.*, 2016, **11**, 327.
50 E. Prodan, C. Radloff, N. J. Halas and P. Nordlander, *Science*, 2003, **302**, 419.
51 V. Pacheco-Peña, M. Beruete, A. I. Fernández-Domínguez, Y. Luo and M. Navarro-Cía, on 9th International Congress on Advanced Electromagnetic Materials in Microwave and Optics, Metamaterials, 2015.
52 X. Liu, X. Xing, Y. Li, N. Chen, I. Djerdj and Y. Wang, *New J. Chem.*, 2015, **39**, 2881.
53 Z. Zeng, C. S. Garoufalis, S. Baskoutas and G. Bester, *Phys. Rev. B: Condens. Matter Mater. Phys.*, 2013, **87**, 125302.
54 L. Novotny and B. Hecht, *Principles of Nano-Optics*, Cambridge University Press, 2012.
55 E. D. Palik, *Handbook of Optical Constants of Solids*, Academic, 1985.
56 I. Bodurov, I. Vlaeva, A. Viraneva, T. Yovcheva and S. Sainov, *Nanosci. Nanotechnol.*, 2016, **16**, 31.